Chapter 6: $NiCo_2O_4$/NiO/MXene as non-precious metal-based electrode for supercapacitor application

6.1. Introduction

The environmental concerns and critical situation of the fossil fuels have attracted the focus of researchers on development of efficient energy storage devices. Among the energy storage devices, supercapacitors have attracted the market in smart grid systems, electrical vehicles and various portable electronic devices owing to its environmental friendliness, high power performance, fast charge-discharge and high cycle life as compared to batteries [1, 2, 3]. The comparatively lower energy density of supercapacitor restrains its further development. As electrode is one of the major components of supercapacitor, so the limitations of supercapacitor can be mitigated by designing efficient electrode material. As charge storage occurs at the electrode-electrolyte interface, so large specific surface area is desirable to obtain good capacitive behaviour. Two-dimensional materials possess large surface area and are considered promising supercapacitor electrodes. Graphene is the most extensively studied two-dimensional material as supercapacitor electrode. In the recent times, MXene is emerging as a potential contender of graphene in supercapacitor. MXenes are two-dimensional layered structures obtained by selectively etching 'A' layer from MAX phase by using wet chemical methods [4]. The name MXene is given to show its analogy with graphene. $M_{n+1}X_nT_x$ is the typical expression for MXene, where M stands for transition metal elements, X for Carbon and/or Nitrogen, and T_x for surface functional groups like O, OH, and F [14]. MXene is regarded as a promising electrode material for supercapacitor due to its exceptional electrical conductivity, layered structure, surface hydrophilicity, electrochemical stability, reversible cation intercalation and presence of variable oxidation states of the transition metal [5, 6]. MXene has strong electrical conductivity around 6000-16,000 Scm^{-1} which is higher than reduced graphene oxide and MoS_2 [6]. The maximum reported specific capacitance obtained with MXene film is 245 Fg^{-1} [7]. However, self- restacking of MXene sheets cause reduction in its effective surface area which inhibits the insertion of electrolyte ions into the surface of the electrode. In this regard, developing hybrids of MXenes with different pseudocapacitive materials like conducting polymers, 2D materials, different transition metal oxides, etc. help reducing

such restacking and regaining the effective surface area. Works have been reported that study the combination of MXenes with single transition metal oxides SnO_2, Fe_3O_4, MnO_2, V_2O_5 [8, 9, 10, 11]; transition metal hydroxides [12]; transition metal chalcogenides [13]; graphene, carbon nanotube [14, 15]; conducting polymer [7,16], etc. For instance, PPy/Ti_3C_2 heterostructure nanocomposite demonstrated a specific capacitance of 458 Fg^{-1} at a scan rate of 2 mVs^{-1}, which was much greater than pure Ti_3C_2 (132 Fg^{-1}) in a 1.0 M H_2SO_4 solution [17]. The hydrophilic functional groups on the ultrathin Ti_3C_2 nanosheets provide nucleophilic reactive sites for polymerization of pyrrole monomers. PPy on the other hand possess good ion wettability, high electrical conductivity and outstanding faradaic pseudocapacitance. Additionally, the combination of PPy nanospheres with Ti_3C_2 nanosheets reduces agglomeration and stacking of Ti_3C_2 layers. Thus, the synergistic contribution of the nanocomposite not only offer extra active sites to PPy, but also prevents PPy nanospheres from agglomeration [17]. The contribution from both EDLC and pseudocapacitance improves the performance of PPy/Ti_3C_2. Another group developed MnO_2-MXene composite, which provided capacitance of 272 F/g at 0.5 A/g in KOH electrolyte, and 165 F/g at the same current density in Na_2SO_4 electrolyte. The asymmetric devices built using MnO_2-MXene as positive electrode and activated carbon as negative electrode offers 1.6 V and 2 V potential window in KOH and Na_2SO_4 electrolytes respectively. The asymmetric device offered energy density of 19.3 Wh/kg and 16.8 Wh/kg respectively in KOH and Na_2SO_4 solutions [18].

In supercapacitor, besides the electrode, electrolytes play a huge role in its performance. An electrolyte with large potential window, good stability and rapid ion transfer is utmost required for optimal performance of the supercapacitor [19]. Liquid electrolytes have good conductivity, fast ion diffusion, low resistance and excellent wetting of electrode surface [20, 21]; however, their practical application is limited due to low ion selectivity, large device dimension, poor portability, leakage of electrolytes and hence high production cost [20, 21]. The operating window of aqueous electrolytes is limited to 1.2 V, whereas the non-aqueous electrolytes can operate up to around 4 V [22], thereby increasing the specific capacitance and energy density of the supercapacitor. The limitations of liquid electrolytes can be overcome by solid/quasi solid-state electrolytes. The solid-state electrolytes offer wide potential window, lightweight, good ionic conductivity, flexibility and are suitable for portable devices [21, 23]. Hydrogels

are the gel polymer electrolytes which are classified as quasi solid-state electrolytes, sometimes called as solid-state electrolytes [24, 25]. Nowadays, studies on flexible and bendable supercapacitors are attracting attention in the field of energy storage applications. Hydrogels can offer excellent mechanical strength and bendability [24]. PVA based hydrogels are the most studied hydrogels in stretchable supercapacitors because of their hydrophilicity, structural integrity, high mechanical stability, chemical resistance, high melting point, and glass transition, which allows the flexible supercapacitors a great variation of bending degree [22, 24, 26].

A nanocomposite of binary mixed metal oxide $NiCo_2O_4$/NiO is developed with MXene in chapter 4. The performance of the nanocomposite $NiCo_2O_4$/NiO/MXene (CNOT) as supercapacitor electrode is evaluated in this chapter. The nanocomposite is designed to attain the synergistic contributions from pseudocapacitive $NiCo_2O_4$ and NiO which exhibit excellent electrochemistry due to the presence of multiple redox active sites and improved conductivity due to the presence of MXene nanosheets. The Vander Waals force between the MXene layers causes MXene nanosheets to restack [27], which can be mitigated by the binary mixed metal oxide $NiCo_2O_4$/NiO. The agglomeration and low conductivity of metal oxides $NiCo_2O_4$/NiO is compensated by MXene nanosheets. The layered structure of MXene renders more active sites to the nanocomposite and the strong interfacial interactions developed between MXene nanosheets and $NiCo_2O_4$/NiO shortens the ion diffusion pathways and fasten the charge transfer within the nanocomposite. A symmetric supercapacitor device is assembled using PVA/KOH hydrogel electrolyte and its performance is compared with aqueous KOH electrolyte. Taking the advantages of large surface area, good chemical stability, conductivity, and hydrophilicity, the nanocomposite provides wide potential window and good capacitance in aqueous as well as hydrogel electrolyte PVA/KOH.

6.2 Experimental section

6.2.1 Electrochemical characterizations:

Electrochemical studies were conducted using three electrode and two-electrode system in Gamry (Model- Gamry Interface 1010 E) at ambient environment. Pt wire (counter), Ag/AgCl (Reference) and graphite foil coated with sample (working electrode) were used for the three-electrode study. Catalyst slurry was prepared by mixing the active material, carbon black and nafion in the ratio of 75:15:10 in isopropanol and DI water. The working

electrodes were prepared by coating the catalyst slurry on graphite foil (1.5 × 1 cm^2). Mass of active material deposited was calculated to be 0.1 mg. Prior to drop casting, graphite foils were washed with ethanol. Cyclic voltammetry, Galvanostatic charge-discharge (GCD), and EIS were performed. The parameters were: - (-0.2 to 0.55) V window for CV, 3 M aqueous KOH solution was used as the electrolyte. The expressions used for calculation of specific capacitance, energy density and power density are mentioned below. The specific capacitance (C_{sp}), energy density (E) and power density (P) of the symmetric supercapacitor are calculated by considering the following relations (equations 6.1-6.3) [28, 29].

$$C_{sp}\ (Fg^{-1}) = \frac{I\,\Delta t}{m\Delta V} \tag{6.1}$$

$$E\ (Whkg^{-1}) = \frac{1}{2} \times C_{cp} \times (\Delta V)^2 \times \frac{1000}{3600} \tag{6.2}$$

$$P\ (Wkg^{-1}) = \frac{E \times 3600}{\Delta t} \tag{6.3}$$

where I is the discharge current in ampere, Δt is the discharging time in second, m is the mass of the active material (in gram) in both the positive and negative electrodes, ΔV is the potential window (in volt). The specific capacitance of the single electrode in three-electrode configuration is measured using relation (1) where m is the mass of active mass in single electrode.

6.3 Results and Discussion

6.3.1 Electrochemical characterizations

6.3.1.1 Three-electrode electrochemical behaviour of the electrodes:

To explore the charge transfer processes of $NiCo_2O_4$/NiO/MXene (CNOT) and MXene, cyclic voltammetry has been performed and 3 M KOH is the optimized electrolyte used for all the electrochemical characterizations. Cyclic voltammetry is performed in the potential window (-0.2 to 0.55) V vs. Ag/AgCl. From fig 6.1a it is observed that CNOT offers higher CV area and current density than MXene and the metal oxides $NiCo_2O_4$ (NCO) and $NiCo_2O_4$/NiO (CNO). Redox peaks are observed in all the electrodes NCO, CNO and CNOT. The area under CV curve of bare graphite is negligibly small, and it does not show any redox peak, which suggests its inactiveness in the charge storage. In the cyclic voltammogram of MXene (in fig. 6.1b), a pair of redox peaks is observed which denotes the pseudocapacitive behaviour of Ti atoms. However, the origin of this

redox peak is still not clearly understood in literature [30, 31]. The almost rectangular shape of MXene CV also suggest its EDLC contribution in addition of its pseudocapacitive behaviour [32, 33]. The redox peaks of NCO, CNO, and CNOT are attributed to the change in oxidation state of Co and Ni in the redox couples Co_3O_4/CoOOH and NiO/NiOOH. The redox reaction governing these peaks is- $NiCo_2O_4 + OH^- + H_2O \rightarrow 2CoOOH + NiOOH + e^-$.

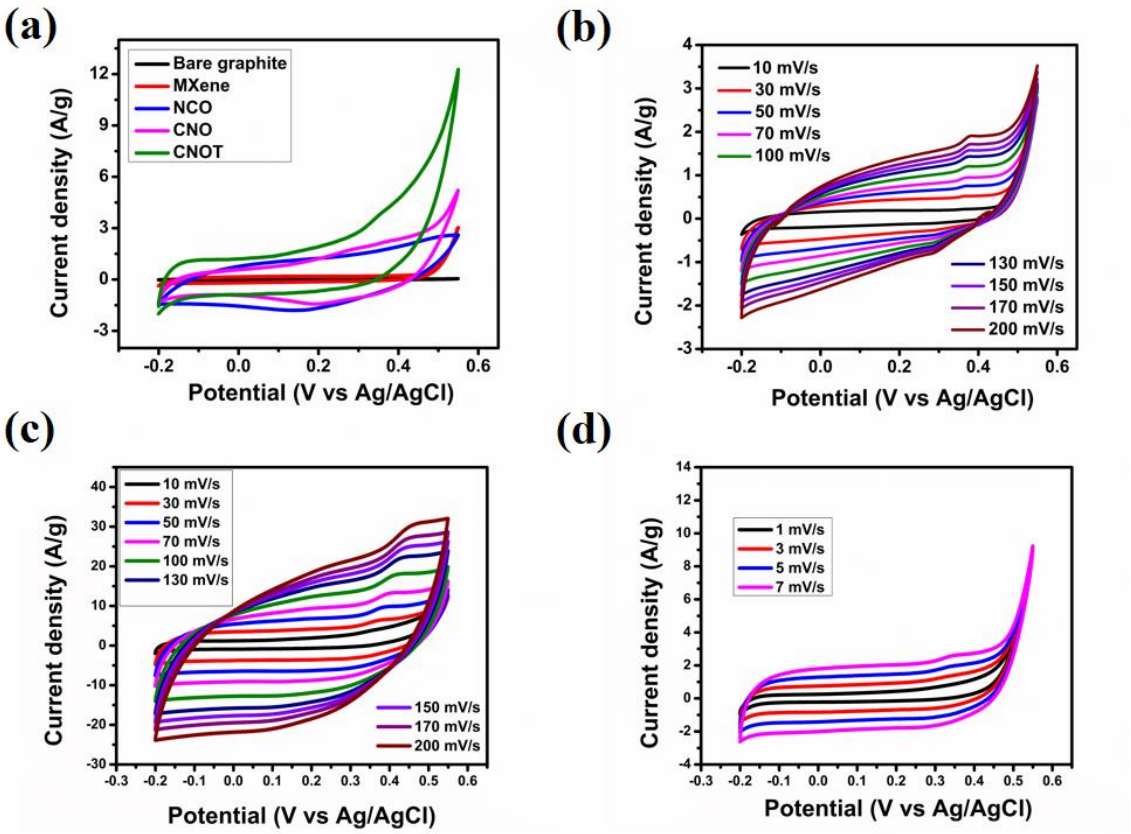

Figure 6.1: 3-electrode electrochemical characterizations in 3M KOH: Cyclic voltammetry of (a) All electrodes at 10 mV/s scan rate, (b) MXene, (c) CNOT at high scan rate, (d) CNOT at low scan rate

Figure 6.1c and 6.1d display the cyclic voltammogram of CNOT at both high and low scan rate, respectively. Due to the presence of MXene nanosheets, the shape of CV is almost rectangular which confirms the EDLC contribution of MXene. A higher current density is obtained for the hybrid electrode CNOT due to the synergistic effect of the individual components. The restacking of MXene nanosheets gets reduced in the nanocomposite CNOT, resulting in higher CV area and current density. The shape of CV

curves remains unchanged even at higher scan rate, which indicates good reversibility and coulombic efficiency of the hybrid CNOT. The contribution of both capacitive and diffusion controlled process in MXene and CNOT, has been verified by the kinetic behaviour of the electrodes, studied by plotting the logarithm of current density with logarithm of scan rate, and by using Dunn's method (the study has been presented in Appendix A).

Galvanostatic charge-discharge was performed for the electrodes in 3 M KOH aqueous solution in the potential window (-0.17 to 0.32) V vs Ag/AgCl. Figure 6.2a shows the GCD curve of MXene, NCO, CNO, and CNOT at 1 A/g current density. All the GCD curves show linearity during charging and discharging process. GCD curves of CNOT appears more symmetrical suggesting better reversibility of the electrode, which is attributed to the EDLC contribution from MXene nanosheets. CNOT exhibits the highest specific capacitance value of 674 Fg^{-1}, whereas CNO, NCO and MXene offer specific capacitance value of 362 Fg^{-1}, 159 Fg^{-1}, and 26 Fg^{-1} respectively at 1 A/g current density. The GCD curves of MXene and CNOT at varying current density from 0.5 to 10 A/g are displayed in fig. 6.2b and 6.2c respectively (The current density varying GCD curves of NCO and CNO are discussed in section 5.3.1.1 of chapter 5). The capacitance of MXene becomes 12.24 Fg^{-1} with capacitance retention of 47.32% at 10 A/g, whereas CNOT offers 63.52% capacitance retention. The presence of NiO in the binary composite $NiCo_2O_4$/NiO leads to more charge transport and storage. The hydrophilic terminations present on the surface of MXene nanosheets help in charge adsorption and enhance the capacitance of the system. However, the capacitance of MXene based electrodes reduces owing to the restacking of these nanosheets, which prevent the effective exposure of the surface to the electrolyte ions. This restacking has been minimised by creating hybrid of these MXene nanosheets with metal oxides $NiCo_2O$/NiO. In the hybrid electrode CNOT, the presence of metal oxide on the surface of MXenes reduces the restacking of the nanosheets, thereby making the surface more accessible to the electrolyte ions. Thus, it reduces the charge transfer resistance offered by the hybrid CNOT, which is evident from the least R_{ct} value in the Nyquist plot shown in fig. 6.2d.

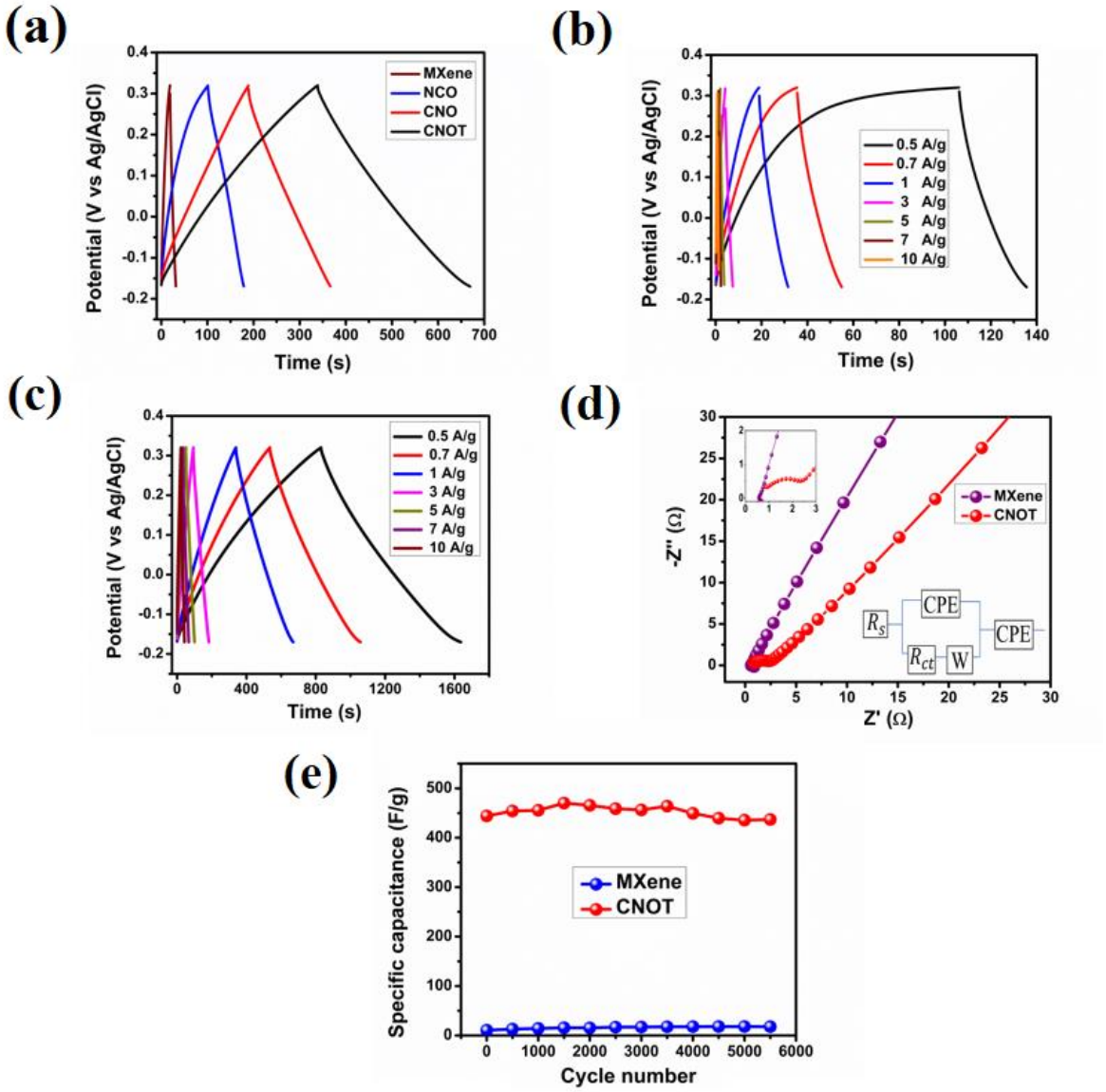

Figure 6.2: 3-electrode electrochemical characterizations in 3M KOH: Galvanostatic charge-discharge of (a) All electrodes at 1 A/g current density, (b) MXene from 0.5 to 10 A/g, (c) CNOT from 0.5 to 10 A/g current density, (d) Nyquist plot (Left inset: magnified view of higher frequency region of Nyquist plot, Right inset: Equivalent circuit), (e) Cycling stability of CNOT at 10 A/g

To investigate the charge transfer processes and the impedances involved, EIS is performed and the Nyquist plots are displayed in fig.6.2d. Experimental data are fitted with equivalent electrochemical electrical circuit comprising of series resistance (R_s), charge transfer resistance (R_{ct}), constant phase element (CPE), and Warburg impedance (W) (circuit shown in inset of fig. 6.2d). The high and intermediate frequency section is

controlled by charge transfer kinetics, and the low frequency section is controlled by ionic diffusion. CNOT offers very less R_s (0.613 Ω), and R_{ct} of 1.848 Ω, whereas MXene offers R_s and R_{ct} of 0.612 Ω and 0.594 Ω respectively. The closely vertical line in the lower frequency side represents Warburg impedance. Low Warburg impedance suggests easy and fast ionic diffusion into the electrode. CNOT offers low Warburg impedance of 0.02141 $Ss^{\frac{1}{2}}$ and MXene offers 0.003451 $Ss^{\frac{1}{2}}$. Thus, excellent conductivity, hydrophilicity, large surface area and good interfacial interaction between MXene nanosheets and $NiCo_2O_4$/NiO, lead to low series and charge transfer resistance of CNOT. Moreover, the hydrophilic groups present on MXene surface lead to decrease in series resistance of CNOT. To understand the stability and capacitive retention of the electrodes, cycling stability of MXene and CNOT have been performed at 10 A/g current density for 5500 GCD cycles (as shown in fig. 6.2e). MXene shows increase in specific capacitance from first cycle (10.5 F/g) to 5500^{th} cycle (17.75 F/g). This increase in capacitance may be due to structural instability of MXene nanosheets during the continuous charging-discharging process. In contrast, CNOT offers an excellent cycling stability with 98.36% capacitive retention after 5500 cycles (observed in fig. 6.2e). The slight decrease in capacitance of CNOT is due to the increase in charge transfer resistance (2.651 Ω, as shown in fig. 6.3a along with the equivalent circuit) after continuous charge-discharge process. The excellent stability of CNOT arises due to the synergistic contribution of MXene and the transition metal oxides $NiCo_2O_4$ and NiO. The strong interfacial interactions among the components reduces the agglomeration and restacking of transition metal oxides and MXene nanosheets respectively, in the nanocomposite. However, after 5500 GCD cycles, the MXene nanosheets restack and get rolled into cylindrical shape, and the $NiCo_2O_4$/NiO nanoparticles agglomerate (as observed from fig. 6.3b and 6.3c), which is the main reason behind increase in charge transfer resistance and the reduction of capacitive response of the nanocomposite after prolonged charge-discharge.

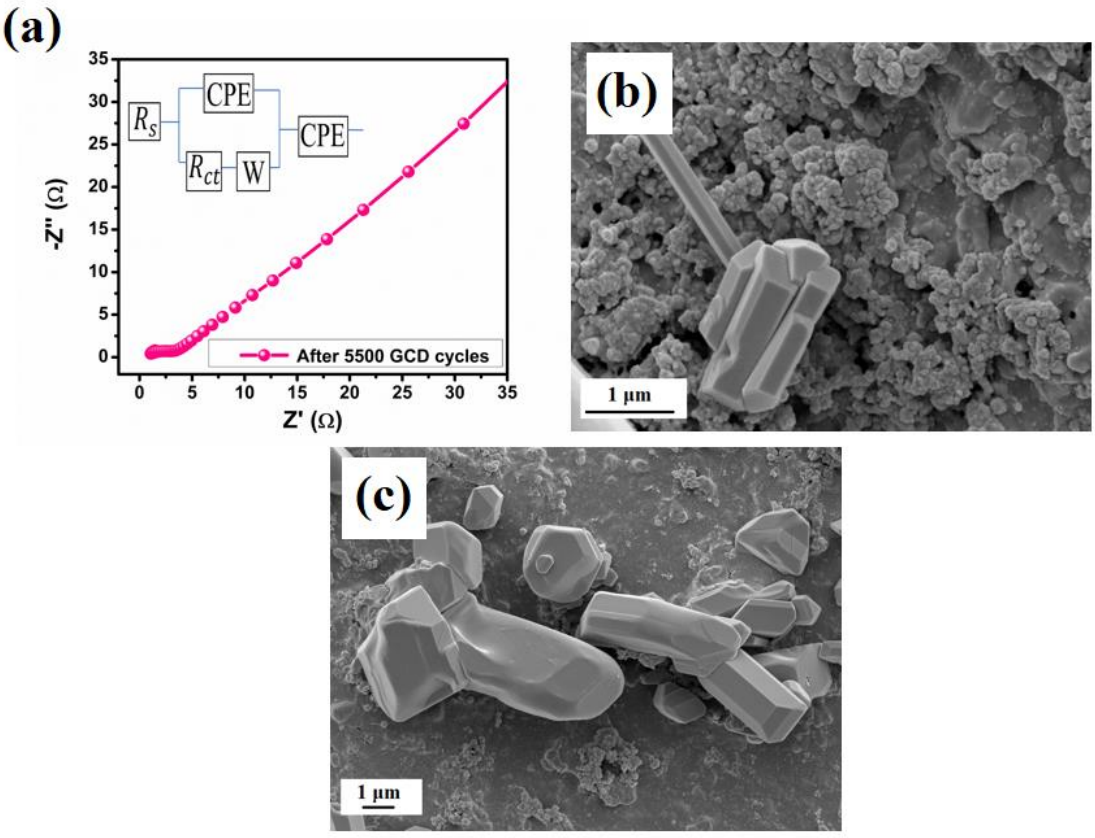

Figure 6.3: Post cycling stability test of CNOT: (a) EIS (Inset: Equivalent circuit), (b)-(c) FESEM images

6.3.1.2 Electrochemical behaviour of the symmetric supercapacitor:

6.3.1.2.1 3M KOH aqueous electrolyte:

To assess the real-life implication of CNOT as supercapacitor, a symmetric supercapacitor is developed using it as cathode and anode in two-electrode system. Cyclic voltammetry of the CNOT//CNOT symmetric device is performed at different potential windows (displayed in fig. 6.4a) to find the optimized window. It is observed from fig. 6.4a that with window exceeding 0.9 V, the current sharply rises, which occurs due to splitting of water to form oxygen. The GCD is also performed in different window to find out the optimum one. From fig. 6.4b it is clearly visible that when potential rises beyond 0.9 V, some side reaction occurs in the electrode, which corroborates well the CV curves. Thus, (0 to 0.9) V is the optimized window, in which the electrode exhibits higher current density. As shown in the CV curve of fig. 6.4c, bare graphite offers

negligible current density as compared to CNOT, which proves the charge storage contribution comes effectively from CNOT.

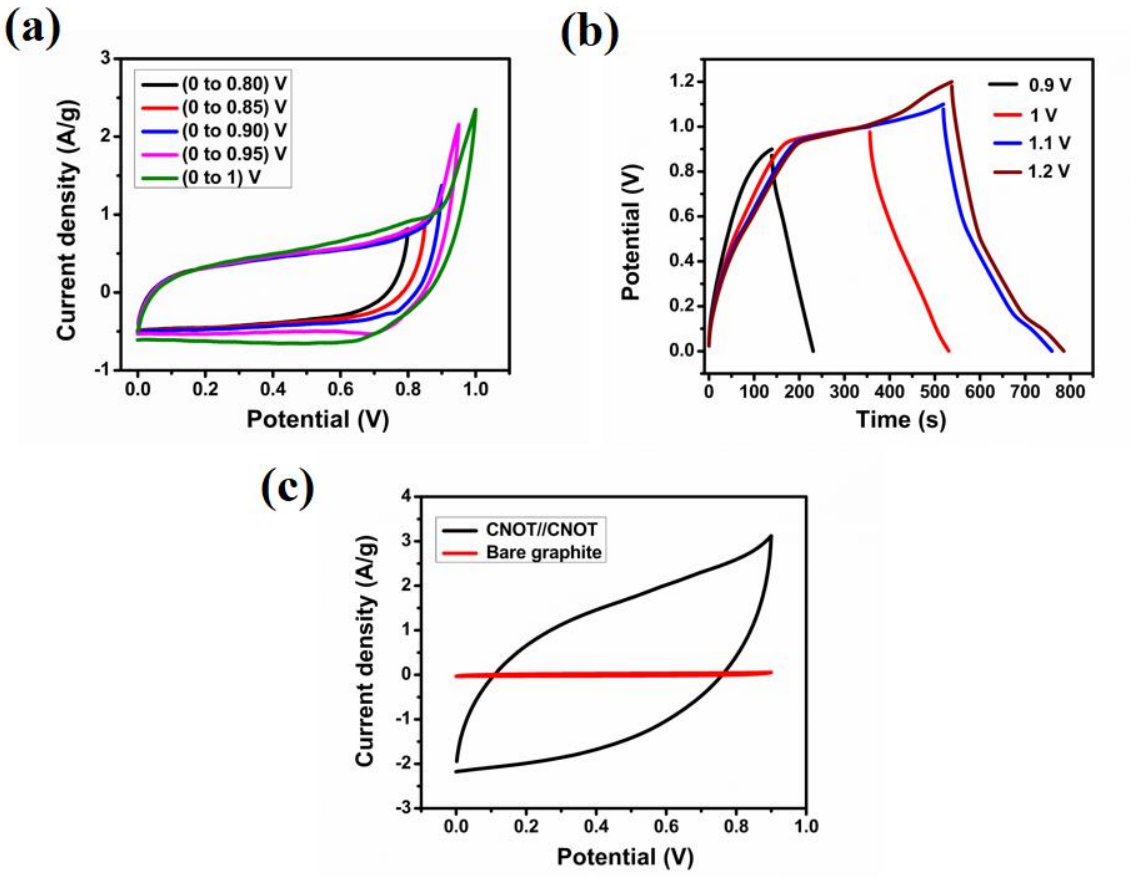

Figure 6.4: Two-electrode electrochemical characterization of symmetric supercapacitor CNOT//CNOT in 3M KOH: (a) Cyclic voltammetry in different potential window, (b) GCD at 0.5 A/g for different potential windows, (c) CV of CNOT//CNOT and bare graphite//bare graphite at 50 mV/s in window (0 to 0.9) V

Fig. 6.5a depicts the CV curves for 0.9 V window at different scan rates. The CV curves are quasi-rectangular with slight oxidation peak observed around 0.5 to 0.7 V. The EDLC contribution from MXene dominates due to which the rectangular shape prevails. The quasi-linearity is also prominent from the GCD curves in fig. 6.5b. With increasing current density from 1.5 to 10 A/g, the decrease in discharge time is obvious due to less time available for the electrolyte ions to diffuse into the catalyst bulk.

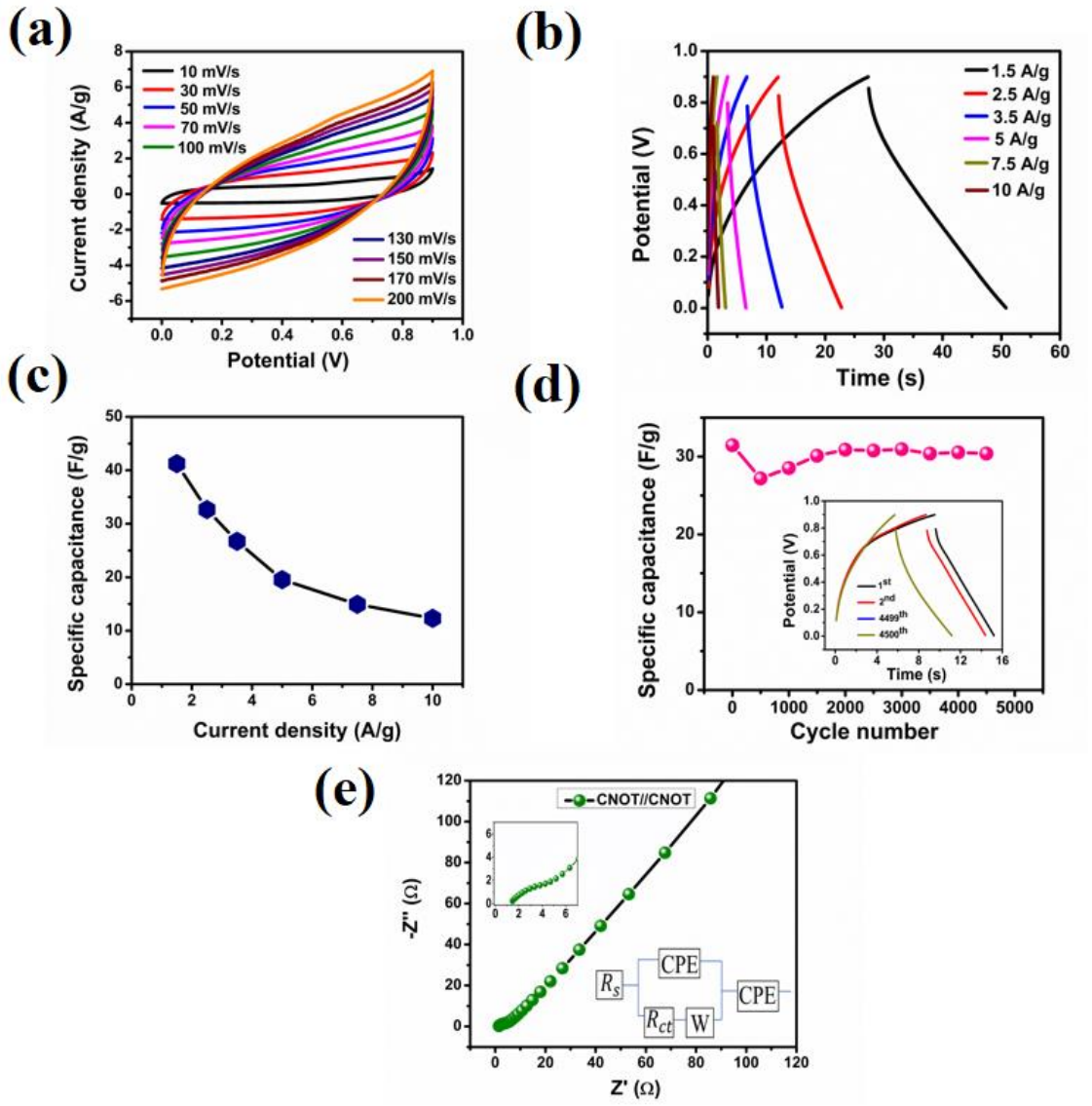

Figure 6.5: Two-electrode electrochemical characterization of symmetric supercapacitor CNOT//CNOT in 3M KOH: (a) Cyclic voltammograms in (0 to 0.9) V with varying scan rate, (b) Galvanostatic charge-discharge at varying current density, (c) Specific capacitance vs. current density plot, (d) Specific capacitance with cycle number (Inset: Two cycles from first and last), (e) Nyquist plots (Left inset: magnified view of the higher frequency region Nyquist plot, Right inset: Equivalent circuit)

Specific capacitance of 41 Fg^{-1} is obtained at 1.5 A/g current density with specific energy and power being 4.6 Wh/kg and 711.5 W/kg respectively. At 10 A/g, the values of specific capacitance, specific energy and power becomes 12.308 Fg^{-1}, 1.384 Wh/kg and 5748.9 W/kg respectively. The specific capacitance retention of CNOT//CNOT at 5 A/g

is found to be 47.38%, which further decreases to 36.2% and 29.84% at 7.5 and 10 A/g, respectively (presented in specific capacitance versus current density plot in fig. 6.5c). It offers coulombic efficiency of 89.35% at 10 A/g current density. The stability of the symmetric supercapacitor is studied by performing GCD at 5 A/g for 4500 cycles (fig. 6.5d). Specific capacitance of 32.33 Fg^{-1} and 27.185 Fg^{-1} is obtained for 1st and 500th cycle respectively, with 84% retention in the 500th cycle. This capacitance increases in the 1000th cycle with retention of 88.2%. The C_{sp} value increases up to 3000 cycles, which reduces to 30.388 Fg^{-1} in the 4500th cycle, with very good capacitive retention of 94%. The hydrophilic terminations -O, -OH, etc. of MXene, attract more electrolyte ions into the electroactive sites, thereby decreasing the charge transfer resistance. The low charge transfer resistance (3 **Ω**) (shown in Nyquist plot fig. 6.5e) offered by the symmetric supercapacitor CNOT//CNOT facilitates easy ion penetration and charge storage.

6.3.1.2.2 PVA/3M KOH gel polymer electrolyte:

In order to develop a potential energy storage device in the market, the potential window has to be improved beyond 0.9 V. Since in aqueous electrolyte, due to the splitting of water molecules into oxygen and hydrogen, the potential is difficult to exceed beyond 1.23 V. To circumvent this drawback of 3 M KOH aqueous solution, a hydrogel electrolyte of PVA and 3M KOH is prepared. A symmetric supercapacitor device is designed using the hydrogel as electrolyte and CNOT as cathode and anode, and its electrochemical studies are displayed in fig. 6.6. Fig. 6.6a depicts the CV curves in different potential window. It is observed that when the potential exceeds beyond 1.4 V, the current sharply increases which may be due to the side reactions taking place in the electrolyte. Thus, 1.4 V is considered the optimized potential in which the CV is done by varying scan rate, shown in fig. 6.6b. With increasing scan rate, the current increases and retains the shape which reveals the reversibility of the electrode in this window at higher scan rate. GCD is performed at current densities from 2.5 to 10 A/g (shown in fig. 6.6c), in which quasi-linear GCD curves are obtained. The symmetric supercapacitor device exhibits a specific capacitance of 87.33 Fg^{-1}, energy and power density of 23.77 Wh/kg and 1808.87 W/kg, respectively at 2.5 A/g. Whereas, at 10 A/g the obtained values are: specific capacitance = 55.916 Fg^{-1}, energy density = 15.22 Wh/kg, and power density = 8184 W/kg. The specific capacitance versus current density plot (in fig. 6.6d) gives

capacitance retention of 84.28%, 71.12% and 64% at 5, 7.5, and 10 A/g current density, respectively. It offers coulombic efficiency of 90.96% at 10 A/g current density.

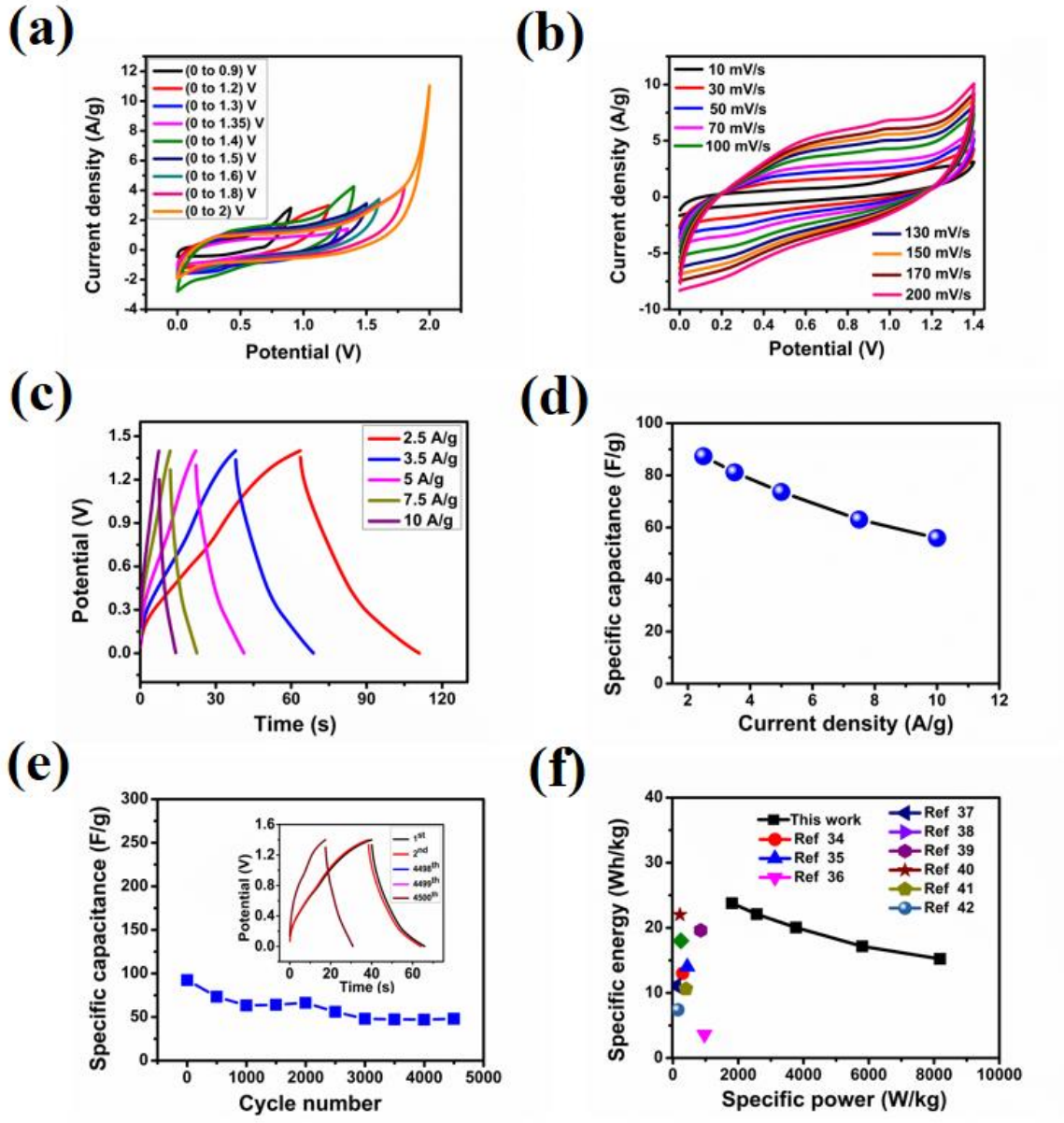

Figure 6.6: Two-electrode electrochemical characterization of symmetric supercapacitor CNOT//CNOT in hydrogel polymer electrolyte PVA/3M KOH: (a) Cyclic voltammetry in different potential window, (b) Cyclic voltammograms in (0 to 1.4) V with varying scan rate, (c) Galvanostatic charge-discharge curves at varying current density, (d) Specific capacitance vs. current density plot, (e) Specific capacitance with cycle number (Inset: First two and last three cycles), (f) Ragone plot

The higher rate capability of the symmetric supercapacitor in hydrogel electrolyte (PVA/KOH) than aqueous (KOH) electrolyte suggests better storage ability in hydrogel. To understand the durability of the developed symmetric device, cycling stability is done for 4500 GCD cycles at 5 A/g and is shown in fig. 6.6e. A retention of 47.9% is obtained after 4500 cycles. The energy density and power density of our developed device are shown in the Ragone plot in fig. 6.6f. Figure 6.6f displays a comparison with other reported works [34-42], from which it is observed that the energy and power density of the present work are better than many other reported symmetric supercapacitors. Thus, CNOT//CNOT based on PVA based hydrogel electrolyte provides higher energy as well as power density, which is due to the synergistic effect of conductivity and hydrophilicity of MXene nanosheets, interfacial interaction among MXene and $NiCo_2O_4$/NiO nanoparticles, and the widened potential window of the PVA-hydrogel electrolyte which offers the electrolyte ions a broad range of potential for storage, thereby increasing its specific capacitance.

The structural changes in the electrode after charge-discharge for 4500 cycles are monitored using XRD (depicted in fig. 6.7a and 6.7b). The XRD peaks of the electrode material get suppressed due to the sharp peaks of graphite at 26.02° and 54° corresponding to (002) and (004) plane (according to JCPDS no. 75-2078) [43]. As observed in fig. 6.7b, upon magnifying, peaks of CNOT are observed at 16.7°, 31.4°, 37°, 43.9°, 65.7°, and 77.13° corresponding to (111), (220), (311), (400), (440), and (533) planes of $NiCo_2O_4$. Peaks arising at 42.7°, 62.59° correspond to NiO planes (200) and (220). Another peak appearing at 60.2° corresponds to (110) plane of MXene nanosheets. Two additional peaks appear at 33.69° and 40.1° owing to (100), (101) plane of $Ni(OH)_2$ (JCPDS 38-0715) [44]; whereas, the peaks at 38.7° and 48.5° represent the (222) and (422) plane of Co_2O_4 respectively (JCPDS 9-418) [45, 46]. The XRD of bare graphite is presented in fig. 6.7c. The formation of $Ni(OH)_2$ during charge-discharge occurs due to the reduction of NiOOH from NiO, according to the equations $NiO + OH^- \rightarrow NiOOH + e^-$ and $NiOOH + H_2O + e^- \rightarrow Ni(OH)_2 + OH^-$. Similarly, Co_2O_4 is formed by decomposition of $NiCo_2O_4$ into Co_2O_4 and NiO.

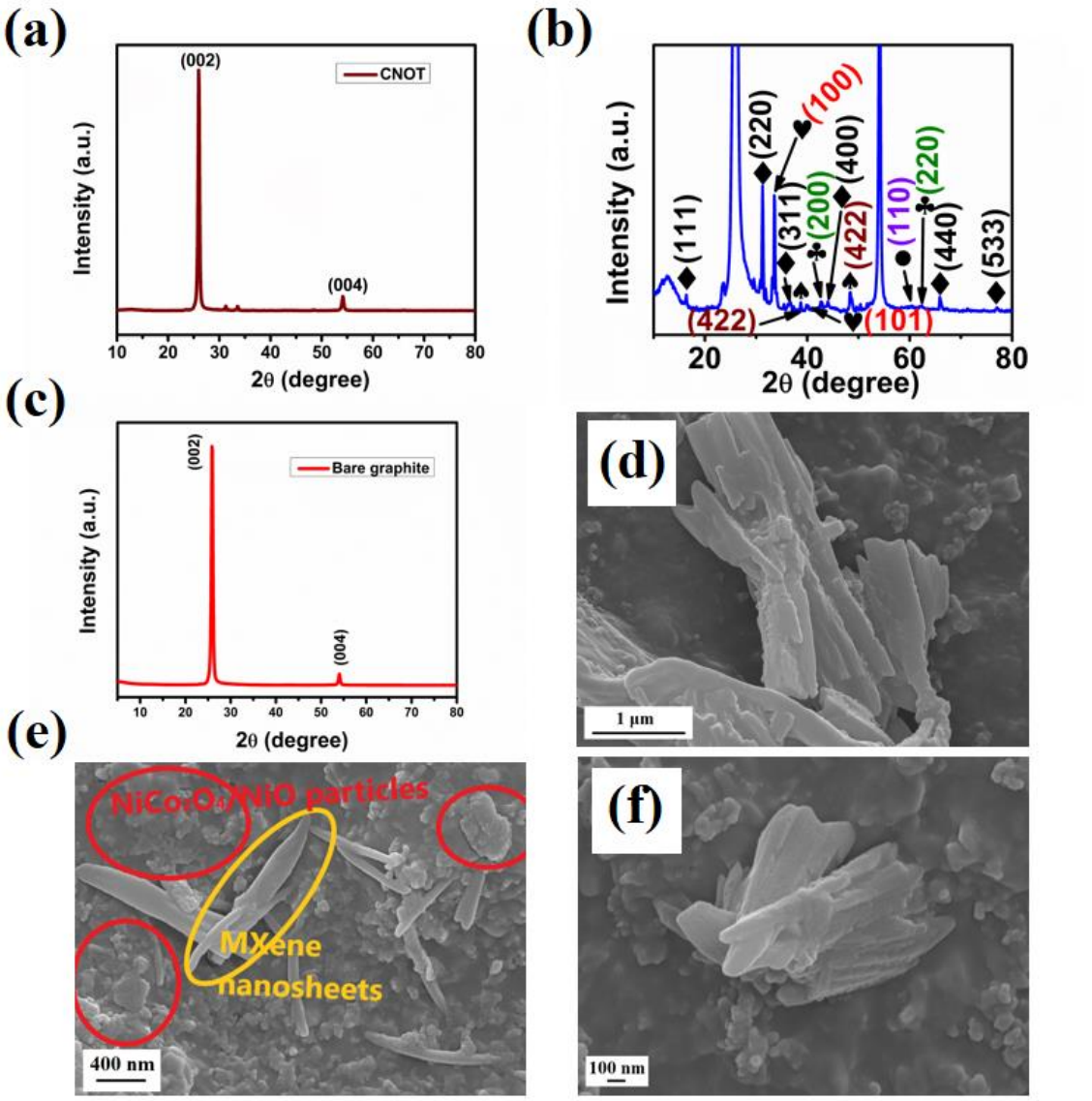

Figure 6.7: Structural and morphological characterization of CNOT after 4500 GCD cycles of the symmetric supercapacitor CNOT//CNOT: (a) XRD pattern of CNOT, (b) Magnified view of XRD peaks of active material; with symbols signifying: ♠ Co_2O_4 ♣ NiO ♥ $Ni(OH)_2$ ♦ $NiCo_2O_4$ phase and ● MXene, (c) XRD of bare graphite, and (d)-(f) FESEM images

After the continuous charging-discharging process, the MXene nanosheets get restacked (as shown in fig. 6.7d, 6.7e, 6.7f) which reduces the exposed surface area of the active material. Figure 6.7e shows the restacking of MXene nanosheets, marked by yellow circles, while the agglomeration of $NiCo_2O_4$/NiO particles can be seen marked by red circles. Due to frequent insertion and withdrawal of electrolyte ions for an extended

period of time, and the restacking of MXene nanosheets, the $NiCo_2O_4$/NiO particles tend to agglomerate. Thus, the agglomeration and restacking of the nanocomposite CNOT after continuous charge-discharge process reduces the effective surface area, interfacial interactions and the available active sites, leading to the reduced specific capacitance of the device.

To validate the practical application of the assembled hydrogel based symmetric supercapacitor cell, 1.8 V LED light has been glowed. 4 cells in series can glow the LED for around 2 minutes 40 seconds. The images of cells connected in series, charging of four cells, and the lit light-emitting diode are shown in fig. 6.8a, 6.8b and 6.8c, 6.8d respectively.

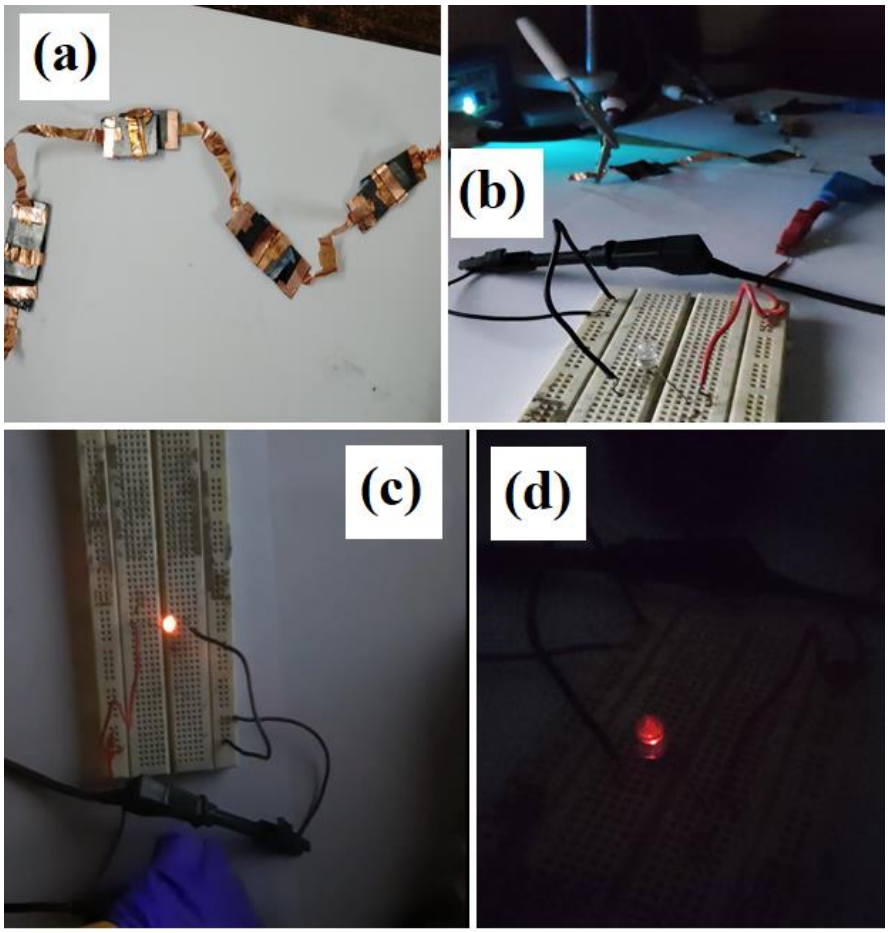

Figure 6.8: Four CNOT//CNOT cells in series, (b) Charging of 4 cells, (c)-(d) 1.8 V LED glow with 4 cells in series

6.4 Conclusion

In summary, this chapter includes the electrochemical characterizations of the developed nanocomposite $NiCo_2O_4$/NiO/MXene (CNOT) and studies its potential as supercapacitor electrode. A two-dimensional conducting material, MXene is explored as possible contender of the extensively studied graphene as supercapacitor electrode. With the unique blend of conductivity, hydrophilicity and large specific surface area, MXene proves its versatility in energy storage and conversion devices. Symmetric supercapacitor device of CNOT is developed using aqueous KOH and PVA based hydrogel electrolyte. The mesoporous nature of the nanocomposite CNOT facilitates facile penetration of electrolyte ions into the electroactive sites of the electrode. The hydrophilic terminations of MXene offer strong interfacial interactions with the transition metal oxides $NiCo_2O_4$ and NiO. This strong interfacial connection among the components increases surface area of the nanocomposite and offer more charge transfer by reducing the ion pathways. The synergistic contribution of MXene and the pseudocapacitive $NiCo_2O_4$ and NiO offers good specific capacitance, and cycle life to the nanocomposite. The hydrophilic terminations formed on the surface of MXene nanosheets during the etching process help in charge storage by EDLC mechanism, thereby increasing the specific capacitance of the electrode. Thus, CNOT as an electrode offers high specific capacitance of 674 Fg^{-1}, excellent cycling stability with 98.36% capacitive retention. The symmetric supercapacitor CNOT//CNOT in aqueous KOH electrolyte offers specific capacitance of 32.66 Fg^{-1} at 2.5 A/g. Whereas, the symmetric supercapacitor device with gel polymer electrolyte outperforms the aqueous KOH electrolyte by providing broader potential window with higher specific capacitance of 87.331 Fg^{-1}, energy density of 23.77 Wh/kg and power density 1808.87 W/kg at 2.5 A/g. Four such cells when connected in series can very well glow a 1.8 V led light for more than 2 minutes. Hence CNOT is a promising candidate for stretchable supercapacitor. It proves its versatility in both energy conversion and storage applications as discussed in chapter 4 and 6 respectively. It can be explored in other fields of electrochemical application as well.

6.5 References:

1. Bhattacharya, K. and Deb, P. Hybrid nanostructured C-dot decorated Fe_3O_4 electrode materials for superior electrochemical energy storage performance. *Dalton Transactions*, 44 (19):9221-9229, 2015.

2. Sharma, M., Ajayan, P.M. and Deb, P. Quantum energy storage in 2D heterointerfaces. *Advanced Materials Interfaces*, 10 (11):2202058, 2023.
3. Talukdar, M., Behera, S.K. and Deb, P. Graphitic carbon nitride decorated with $FeNi_3$ nanoparticles for flexible planar micro-supercapacitor with ultrahigh energy density and quantum storage capacity. *Dalton Transactions*, 48 (32):12137-12146, 2019.
4. Pershaanaa, M., Kamarulazam, F., Gerard, O., Goh, Z.L., Bashir, S., Baruah, K., Deb, P., Ramesh, S. and Ramesh, K. MXenes and their transformation to composites for potential applications. *Materials Today Communications*, 35:106143, 2023.
5. Wang, X., Li, H., Li, H., Lin, S., Ding, W., Zhu, X., Sheng, Z., Wang, H., Zhu, X. and Sun, Y. 2D/2D 1T-MoS_2/Ti_3C_2 MXene heterostructure with excellent supercapacitor performance. *Advanced Functional Materials*, 30 (15):0190302, 2020.
6. Hu, M., Zhang, H., Hu, T., Fan, B., Wang, X. and Li, Z. Emerging 2D MXenes for supercapacitors: status, challenges and prospects. *Chemical Society Reviews*, 49 (18):6666-6693, 2020.
7. Boota, M., Anasori, B., Voigt, C., Zhao, M.Q., Barsoum, M.W. and Gogotsi, Y. Pseudocapacitive electrodes produced by oxidant-free polymerization of pyrrole between the layers of 2D titanium carbide (MXene). *Adv. Mater*, 28 (7):1517-1522, 2016.
8. Ahmed, B., Anjum, D.H., Gogotsi, Y. and Alshareef, H.N. Atomic layer deposition of SnO_2 on MXene for Li-ion battery anodes. *Nano Energy*, 34:249-256, 2017.
9. Zhang, L., Wang, Z., Chen, W., Yuan, R., Zhan, K., Zhu, M., Yang, J. and Zhao, B. Fe_3O_4 nanoplates anchored on $Ti_3C_2T_x$ MXene with enhanced pseudocapacitive and electrocatalytic properties. *Nanoscale*, 13 (36):15343-15351, 2021.
10. Rakhi, R.B., Ahmed, B., Anjum, D. and Alshareef, H.N. Direct chemical synthesis of MnO_2 nanowhiskers on transition-metal carbide surfaces for supercapacitor applications. *ACS applied materials & interfaces*, 8 (29):18806-18814, 2016.

11. Wang, Z., Yu, K., Gong, S., Du, E. and Zhu, Z. Vanadium based carbide–oxide heterogeneous V_2O_5@ V_2C nanotube arrays for high-rate and long-life lithium–sulfur batteries. *Nanoscale*, 12 (36):18950-18964, 2020.
12. Dong, B., Li, W., Huang, X., Ali, Z., Zhang, T., Yang, Z. and Hou, Y.vFabrication of hierarchical hollow Mn doped Ni $(OH)_2$ nanostructures with enhanced catalytic activity towards electrochemical oxidation of methanol. *Nano Energy*, 55:37-41, 2019.
13. Zhan, W., Ma, L., Gan, M. and Xie, F. Ultra-fine bimetallic FeCoP supported by N-doped MWCNTs Pt-based catalyst for efficient electrooxidation of methanol. *Applied Surface Science*, 585:152621, 2022.
14. Yan, J., Ren, C.E., Maleski, K., Hatter, C.B., Anasori, B., Urbankowski, P., Sarycheva, A. and Gogotsi, Y. Flexible MXene/graphene films for ultrafast supercapacitors with outstanding volumetric capacitance. *Advanced Functional Materials*, 27 (30):1701264, 2017.
15. Huang, J.J., Liu, X.Q., Meng, F.F., He, L.Q., Wang, J.X., Wu, J.C., Lu, X.H., Tong, Y.X. and Fang, P.P. A facile method to produce MoSe2/MXene hybrid nanoflowers with enhanced electrocatalytic activity for hydrogen evolution. J. Electroanal. Chem., 856:113727, 2020.
16. Dall'Agnese, Y., Rozier, P., Taberna, P.L., Gogotsi, Y. and Simon, P. Capacitance of two-dimensional titanium carbide (MXene) and MXene/carbon nanotube composites in organic electrolytes. J. Power Sources, 306:510-515, 2016.
17. Wei, D., Wu, W., Zhu, J., Wang, C., Zhao, C. and Wang, L. A facile strategy of polypyrrole nanospheres grown on Ti_3C_2-MXene nanosheets as advanced supercapacitor electrodes. *J. Electroanal. Chem*., 877:114538, 2020.
18. Zhu, Y., Rajouâ, K., Le Vot, S., Fontaine, O., Simon, P. and Favier, F. MnO_2-MXene composite as electrode for supercapacitor. *J. Electrochem. Soc*., 169 (3):030524, 2022.
19. Cao, C., Chu, Y., Zhou, Y., Zhang, C. and Qu, S. Recent advances in stretchable supercapacitors enabled by low-dimensional nanomaterials. *Small*, 14 (52):1803976. 2018.

20. Zhong, C., Deng, Y., Hu, W., Qiao, J., Zhang, L. and Zhang, J. A review of electrolyte materials and compositions for electrochemical supercapacitors. *Chem. Soc. Rev*., 44 (21):7484-7539, 2015.
21. Du, W., Zhang, Z., Du, L., Fan, X., Shen, Z., Ren, X., Zhao, Y., Wei, C. and Wei, S. Designing synthesis of porous biomass carbon from wheat straw and the functionalizing application in flexible, all-solid-state supercapacitors. *J. Alloys Compd*., 797:1031-1040, 2019.
22. Sampath, S., Choudhury, N.A. and Shukla, A.K. Hydrogel membrane electrolyte for electrochemical capacitors. *J. Chem. Sci.*, 121:727-734, 2009.
23. Wang, K., Xu, M., Gu, Y., Gu, Z. and Fan, Q.H. Symmetric supercapacitors using urea-modified lignin derived N-doped porous carbon as electrode materials in liquid and solid electrolytes. *J. Power Sources*, 332:180-186, 2016.
24. Amaral, M.M., Venancio, R., Peterlevitz, A.C. and Zanin, H.J. Recent advances on quasi-solid-state electrolytes for supercapacitors, *J. Energy Chem*., 67:697-717 (2022).
25. Gunasekaran, S.S. and Badhulika, S. High-performance solid-state supercapacitor based on sustainable synthesis of meso-macro porous carbon derived from hemp fibres via CO_2 activation. *J. Energy Storage*, 41:102997, 2021.
26. An, T. and Cheng, W. Recent progress in stretchable supercapacitors. *J. Mater. Chem. A*, 6(32):15478-15494, 2018.
27. Ghidiu, M., Lukatskaya, M.R., Zhao, M.Q., Gogotsi, Y. and Barsoum, M.W. Conductive two-dimensional titanium carbide 'clay' with high volumetric capacitance. *Nature*, 516 (7529):78-81, 2014.
28. Ghosh, K., Yue, C.Y., Sk, M.M., Jena, R.K. and Bi, S. Development of a 3D graphene aerogel and 3D porous graphene/MnO_2@ polyaniline hybrid film for all-solid-state flexible asymmetric supercapacitors. *Sustainable Energy Fuels*, 2 (1):280-293, 2018.
29. Shukla, P.S., Agrawal, A., Gaur, A. and Varma, G.D. Synthesis of mesoporous Zn-doped $MnCo_2O_4$ nanoparticles for high-energy density solid-state asymmetric supercapacitor. *J. Energy Storage*, 73:109229, 2023.
30. Wang, W., Chen, G., Kong, W., Chen, J., Pu, L., Gong, J., Zhang, H. and Dai, Y. Sandwich-like high-performance $Ti_3C_2T_x$ MXene/$NiCo_2O_4$ nanosphere

composites for asymmetric supercapacitor application. *J. Energy Storage*, 86:111097, 2024.

31. Li, Y., Wang, S., Ni, G. and Li, Q. Facile synthesis of $NiCo_2O_4$ nanowire arrays/few-layered Ti_3C_2-MXene composite as binder-free electrode for high-performance supercapacitors. *Molecules*, 27 (19):6452, 2022.
32. Gao, Y., Wang, L., Li, Z., Zhang, Y., Xing, B., Zhang, C. and Zhou, A. Electrochemical performance of Ti_3C_2 supercapacitors in KOH electrolyte. *J. Adv. Ceram.*, 4:130-134, 2015.
33. Wei, D., Wu, W., Zhu, J., Wang, C., Zhao, C. and Wang, L. A facile strategy of polypyrrole nanospheres grown on Ti_3C_2-MXene nanosheets as advanced supercapacitor electrodes. *J. Electroanal. Chem.*, 877:114538, 2020.
34. Yu, D., Ma, Y., Chen, M. and Dong, X. KOH activation of wax gourd-derived carbon materials with high porosity and heteroatom content for aqueous or all-solid-state supercapacitors. *J. Colloid Interface Sci.*, 537:569-578, 2019.
35. Du, W., Zhang, Z., Du, L., Fan, X., Shen, Z., Ren, X., Zhao, Y., Wei, C. and Wei, S. Designing synthesis of porous biomass carbon from wheat straw and the functionalizing application in flexible, all-solid-state supercapacitors. *J. Alloys Compd.*, 797:1031-1040, 2019.
36. Tomar, A.K., Singh, G. and Sharma, R.K. Charge storage characteristics of mesoporous strontium titanate perovskite aqueous as well as flexible solid-state supercapacitor cell. *J. Power Sources*, 426:223-232, 2019.
37. Ma, T., Zhang, X. and Wang, Y. Tassel tree flowers-derived hierarchically porous carbons with high surface area for high-performance flexible all-solid-state symmetric supercapacitors. *J. Energy Storage*, 26:101014, 2019.
38. Shi, W., Chang, B., Yin, H., Zhang, S., Yang, B. and Dong, X. Crab shell-derived honeycomb-like graphitized hierarchically porous carbons for satisfactory rate performance of all-solid-state supercapacitors. *Sustainable Energy Fuels*, 3 (5):1201-1214, 2019.
39. Sharma, M., Hussain, N., Mohanty, S., Puzari, P., Deb, P. Robust energy storage performance enabled by the interacting interface of an epitaxial hybrid nanostructure based flexible supercapacitor. *J. Energy Storage*, 72:108345, 2023.

40. Jiang, L., Sheng, L., Chen, X., Wei, T., Fan, Z. Construction of Nitrogen-doped Porous Carbon Building by Interconnected Ultra-small Carbon Nanosheets for Ultra-high Rate Supercapacitors. *J. Mater. Chem. A*, 4:11388-11396, 2016.
41. Zhang, Y., Sun, Q., Xia, K., Han, B., Zhou, C., Gao, Q., Wang, H., Pu, S., Wu, J. Facile Synthesis of Hierarchically Porous N/P Codoped Carbon with Simultaneously High-Level Heteroatom-Doping and Moderate Porosity for High-Performance Supercapacitor Electrodes, *ACS Sustainable Chem. Eng*., 7:5717-5726, 2019.
42. He, J., Zhang, D., Wang, Y., Zhang, J., Yang, B., Shi, H., Wang, K., Wang, Y. Biomass-derived porous carbons with tailored graphitization degree and pore size distribution for supercapacitors with ultra-high rate capability, *Applied Surface Science*, 515:146020, 2020.
43. Sarmah, D. and Kumar, A. Symmetric Supercapacitors with layer-by-layer Molybdenum disulfide-reduced graphene oxide structures and poly (3, 4-ethylenedioxythiophene) nanoparticles nanohybrid electrode. *J. Energy Storage*, 35:102289, 2021.
44. Rathore, D., Sharma, M.D., Sharma, A., Basu, M. and Pande, S. Aggregates of $Ni/Ni(OH)_2$/NiOOH nanoworms on carbon cloth for electrocatalytic hydrogen evolution. *Langmuir*, 36(46):14019-14030, 2020.
45. Khan, M.I., Muhammad, N., Tariq, M., Nishan, U., Razaq, A., Saleh, T.A., Haija, M.A., Ismail, I. and Rahim, A. Non-enzymatic electrochemical dopamine sensing probe based on hexagonal shape zinc-doped cobalt oxide ($Zn\text{-}Co_2O_4$) nanostructure. *Microchimica Acta*, 189:1-12, 2022.
46. Raza, M.A., Kanwal, Z., Riaz, S. and Naseem, S. Synthesis, characterization and antibacterial properties of nano-sized cobalt particles. In Proceedings of the 2016 World Congress on Advances in Civil, Enviromental, and Materials Research (ACEM16), Jeju Island, Korea, vol. 28, 2016.